Dust and gas power spectrum in M 33 (HERM33ES)

Combes, F.; Boquien, M.; Kramer, C.; Xilouris, E. M.; Bertoldi, F.; Braine, J.; Buchbender, C.; Calzetti, D.; Gratier, P.; Israel, F.

Published in:
Astronomy & astrophysics

DOI:
10.1051/0004-6361/201118282

Publication date:
2012

Astronomy & Astrophysics manuscript no. m33-fourier
January 13, 2012

Dust and gas power-spectrum in M33 (HERM33ES)⋆

F. Combes[1], M. Boquien[2], C. Kramer[3], E. M. Xilouris[4], F. Bertoldi[5], J. Braine[6], C. Buchbender[3], D. Calzetti[7], P. Gratier[8], F. Israel[9], B. Koribalski[10], S. Lord[11], G. Quintana-Lacaci[3], M. Relaño[12], M. Röllig[13], G. Stacey[14], F. S. Tabatabaei[15], R. P. J. Tilanus[16], F. van der Tak[17], P. van der Werf[9], and S. Verley[12]

[1] Observatoire de Paris, LERMA (CNRS:UMR8112), 61 Av. de l'Observatoire, F-75014, Paris, France e-mail: francoise.combes@obspm.fr
[2] Laboratoire d'Astrophysique de Marseille, UMR 6110 CNRS, 38 rue F. Joliot-Curie, 13388, Marseille, France
[3] Instituto Radioastronomia Milimetrica, Av. Divina Pastora 7, Nucleo Central, E-18012 Granada, Spain
[4] Institute of Astronomy and Astrophysics, National Observatory of Athens, P. Penteli, 15236 Athens, Greece
[5] Argelander Institut für Astronomie. Auf dem Hügel 71, D-53121 Bonn, Germany
[6] Laboratoire d'Astrophysique de Bordeaux, Université Bordeaux 1, Observatoire de Bordeaux, OASU, UMR 5804, CNRS/INSU, B.P. 89, Floirac F-33270, France
[7] University of Massachusetts, Department of Astronomy, LGRT-B 619E, Amherst, MA 01003, USA
[8] IRAM-Institut de Radio Astronomie Millimétrique, 300 Rue de la Piscine, 38406-St. Martin d'Hères, France
[9] Leiden Observatory, Leiden University, PO Box 9513, NL 2300 RA Leiden, The Netherlands
[10] ATNF, CSIRO, PO Box 76, Epping, NSW 1710, Australia
[11] IPAC, MS 100-22 California Institute of Technology, Pasadena, CA 91125, USA
[12] Dept. Física Teórica y del Cosmos, Universidad de Granada, Spain
[13] KOSMA, I. Physikalisches Institut, Universität zu Köln, Zülpicher Straße 77, D-50937 Köln, Germany
[14] Department of Astronomy, Cornell University, Ithaca, NY 14853, USA
[15] Max Planck Institut für Astronomie, Königstuhl 17, D-69117 Heidelberg, Germany
[16] JAC, 660 North A'ohoku Place, University Park, Hilo, HI 96720, USA
[17] SRON Netherlands Institute for Space Research, Landleven 12, 9747 AD Groningen, The Netherlands

Received 16 October 2011/ Accepted 10 January 2012

ABSTRACT

Power spectra of de-projected images of late-type galaxies in gas and/or dust emission are very useful diagnostics of the dynamics and stability of their interstellar medium. Previous studies have shown that the power spectra can be approximated as two power-laws, a shallow one at large scale (larger than 500 pc) and a steeper one at small scale, with the break between the two corresponding to the line-of-sight thickness of the galaxy disk. The break separates the 3D behaviour of the interstellar medium at small scale, controlled by star formation and feedback, from the 2D behaviour at large scale, driven by density waves in the disk. The break between these two regimes depends on the thickness of the plane which is determined by the natural self-gravitating scale of the interstellar medium. We present a thorough analysis of the power spectra of the dust and gas emission at several wavelengths in the nearby galaxy M33. In particular, we use the recently obtained images at five wavelengths by PACS and SPIRE onboard *Herschel*. The large dynamical range (2-3 dex in scale) of most images allows us to determine clearly the change in slopes from -1.5 to -4, with some variations with wavelength. The break scale is increasing with wavelength, from 100 pc at 24 and 100μm to 350 pc at 500μm, suggesting that the cool dust lies in a thicker disk than the warm dust, may be due to star formation more confined to the plane. The slope at small scale tends to be steeper at longer wavelength, meaning that the warmer dust is more concentrated in clumps. Numerical simulations of an isolated late-type galaxy, rich in gas and with no bulge, like M33, are carried out, in order to better interpret these observed results. Varying the star formation and feedback parameters, it is possible to obtain a range of power-spectra, with two power-law slopes and breaks, which nicely bracket the data. The small-scale power-law is indeed reflecting the 3D behaviour of the gas layer, steepening strongly while the feedback smoothes the structures, by increasing the gas turbulence. M33 appears to correspond to a fiducial model with an SFR of ~ 0.7 M$_\odot$/yr, with 10% supernovae energy coupled to the gas kinematics.

Key words. galaxies: individual: M33 – galaxies: spiral – galaxies: infrared – galaxies: star formation

1. Introduction

Quantifying the multi-scale structure of the interstellar medium (ISM) in galaxies is a difficult enterprise, but rewarding since it betrays the underlying physical phenomena, controlling its dynamics. It has been known for a long time that the ISM reveals no preferential scale and is well represented by a fractal structure, or a power-law power-spectrum. To study the atomic ISM, Crovisier & Dickey (1983) and Green (1993) studied the power-spectrum as a function of inverse scale of the 21cm emission, and found a power-law of slope between -2 and -3, independent of the distance and the velocity of the HI. This power-law slope was observed to be steeper from -3 to -4, when the broadest velocities were averaged, thus including the warm gas, with more turbulence (Dickey et al. 2001). Goldman (2000) and Stanimirovic et al. (2000) extended the ISM studies in the Milky Way to the Small Magellanic Cloud (SMC), where a power-law of slope -3.1 to -3.4 was found for the dust and gas, and

Send offprint requests to: F. Combes

⋆ *Herschel* is an ESA space observatory with science instruments provided by European–led Principal Investigator consortia and with important participation from NASA.

interpreted as 3D turbulence, although the index is shallower than the -3.7 Kolmogorov spectrum (Stanimirovic & Lazarian 2001). A break in scale has been searched for in order to identify the energy injection mechanism, but none has been found at small scale (i.e. smaller than 500 pc). Instead a flattening towards larger scales has been measured by Elmegreen et al. (2001) in the atomic gas of the Large Magellanic Cloud (LMC). They interpret this flattening as a change of dimensionality, from 3D at small scale to 2D at large scale, where the dynamics of the galaxy plane is dominating, and identify the scale of the break as the thickness of the plane. This method to find the scale height of disks has been developed by Padoan et al. (2001), who found $\sim$ 180 pc in the LMC. Recently, Block et al. (2010) have analysed the dust maps of the LMC from Spitzer, and also confirm this break scale at 100-200 pc. From high resolution numerical simulations fitted to a late-type galaxy like the LMC, Bournaud et al. (2010) were able to retrieve the characteristics of the observed dust power-spectrum. The source of turbulence could then be due to large-scale differential rotation, cold gas accretion or galaxy interactions (Lazarian et al. 2001, Elmegreen & Scalo 2004). Khalil et al. (2006), from a 2D wavelet analysis of HI in our own Galaxy, find a power-law slope of -3 everywhere over the second quadrant, and do not detect the variations with velocity slices predicted by Lazarian & Pogosyan (2004). However they discover an anisotropy linked to spiral arms. The fractal approach was widely developed for molecular clouds, which are more self-gravitating than the HI gas (Falgarone et al. 1991, Pfenniger & Combes 1994, Stutzki et al. 1998).

Up to now, the break scale in the HI distribution has not been identified unambiguously in external galaxies other than the LMC, although it has been searched for. Dutta et al. (2008) studied the face-on galaxy NGC 628, and found an HI power spectrum with a single power-law slope of -1.6, over the scales 0.8 to 8 kpc, their spatial resolution being insufficient to reach the scale height of the gaseous plane. In DDO210, Begum et al. (2006) found a power-law slope of -2.75 over the scales 80 to 500 pc. This steep slope is compatible with what is found in the MW and LMC/SMC at small scales, driven by 3D-turbulence. In other dwarfs also (Dutta et al. 2009b) a single slope is found. The face-on galaxy NGC1058 is the first one for which the transition from 3D to 2D turbulence has been claimed (Dutta et al. 2009a): the slope changes from -2.5 over 0.6 to 1.5 kpc, to -1 over 1.5-10 kpc scales. The scale height is then estimated at 490 pc, which is a relatively large value for the HI layer. In the SMC, while a steep power-law is found consistently by several studies, no break scale has been found, and no transition to the 2D-turbulence (Roychowdhury et al. 2010). It is suggested that dwarf galaxies have gas disks considerably thicker than normal spiral galaxies, which support previous studies from the thickness of dust lanes in edge-on galaxies (e.g. Dalcanton et al. 2004). The transition between thick and thin gas disks was found at a mass corresponding to a circular velocity of 120 $\mathrm{km\,s^{-1}}$. For galaxies with low inclination on the sky plane, the thickness of gas disks can be estimated through the ratio of gas velocity dispersion to rotation (Dalcanton & Stilp 2010). The case of M33 is exactly intermediate, having a rotational velocity of 120 $\mathrm{km\,s^{-1}}$. Both thick and thin disks could be expected.

Another tool to explore the scale height of disks with higher spatial resolution, apart from studying edge-on galaxies (e.g. Bianchi & Xilouris 2011), is to study young components related to the gas, as young stars just formed out of the ISM. Elmegreen et al. (2003a) studied the power-spectrum of star formation maps in nearby galaxies, and found the same behaviour as for the LMC in HI: a steep power-law at small scales, typical of 3D-turbulence, with a flattening at large scales, and a break corresponding to several hundred parsecs, typical of the plane thickness. This is true for flocculent and density-wave galaxies, although the spiral arm wave dominates at very large scales. In M33, Elmegreen et al. (2003b) analysed optical and Hα images and found a very shallow power-law of slope -0.7, which they attribute to flattening due to contamination by strong point sources (foreground stars). For the face-on galaxy NGC 628, a shallow slope of -1.5 is found, with no break in spite of the very high spatial resolution obtained with HST (scale below 10 pc, Elmegreen et al. 2006). Odekon (2008) however finds a transition scale of about 300 pc between a steep spectrum at small scale and flattening at large scale, in the stellar distribution of M33. This scale does not change much with the age of the stellar population considered, however the slope is steeper for the bluest and youngest stars. Sanchez et al. (2010) investigate all the young components in M33, including young stars, HII regions and molecular clouds, and also find a clear transition region, but in the range 0.5-1 kpc. The fact that different results are obtained for the same galaxies calls for new studies to clarify the situation.

The galaxy M33 has been observed with *Herschel* PACS and SPIRE at all wavelengths, by the Key Project HERM33ES, and the photometric maps have been presented in Kramer et al. (2010), Boquien et al. (2010) and Verley et al. (2010). These provide high signal-to-noise maps with a large dynamical range of scales of the dust emission at many wavelength, allowing to probe warm and cool dust. The large and small scale structures of the gas and dust are studied through Fourier analysis. We present in Section 2 the different maps used, and how they are processed, and deprojected to a face-on orientation. The results will be compared to numerical models, which technique is described in Section 3. Results are presented for both observations and models in Section 4, and discussed in Section 5. We adopt a distance of 840 kpc for M33 (Freedman et al. 1991).

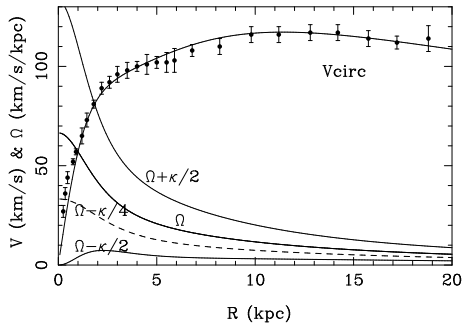

Fig. 1. Rotation curve for our late-type Scd model, compared to the observed points (symbols and error bars) compiled for M33 by Corbelli & Salucci (2007). In addition to the circular velocity of the model, the characteristic frequencies Ω, $\Omega - \kappa/2$, etc. are plotted.

2. Observational data

To study the interstellar medium structure, we use all possible tracers, beginning by gas and dust emission (HI, CO lines, and far-infrared photometry), and also star formation from the gas (Hα, ultra-violet continuum).

For the dust emission, we use *Herschel* observations taken in the context of the HERM33ES open time key project (Kramer

Table 1. Characteristics of the different maps used

Map	Resolution		Npix	pixel size	
	(″)	(pc)		(″)	(pc)
Galex-FUV	4.3”	17	2560	1.5”	6
Galex-NUV	5.3”	21	2560	1.5”	6
Hα	6”	24	1920	2”	8
MIPS-24μm	6”	24	2560	1.5”	6
MIPS-70μm	18”	72	850	4.5”	18
PACS-100μm	7”	28	2268	1.7”	7
PACS-160μm	11”	44	1344	2.85”	12
SPIRE-250μm	18”	72	800	6”	24
SPIRE-350μm	26”	104	480	10”	41
SPIRE-500μm	36”	144	342	14”	57
CO(2-1)	12”	48	1470	2”	8
HI-21cm	12”	48	1200	4”	16

A distance of 840 kpc has been adopted for M33. 1” = 4 pc
Resolutions correspond to the major axis direction,
they are 1/cos(56°) = 1.79 larger in the other direction
Npix is the number of pixels in each dimension of the map

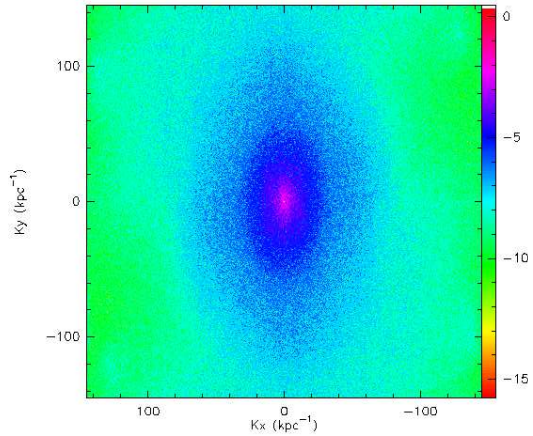

Fig. 2. 2D power-spectrum for the PACS 100μm image. The color scale is in arbitrary units.

et al. 2010) in combination with Spitzer MIPS data (Verley et al. 2007), spanning wavelengths from 24μm to 500μm.

The *Herschel* PACS data covering the 100μm and 160μm bands, have been described in Boquien et al. (2010, 2011). The SPIRE observations obtained at 250, 350 and 500μm are displayed in Kramer et al. (2010) and Verley et al. (2010).

We also use ground-based Hα observations presented in Hoopes et al. (2001) in order to trace the current (∼ 10 Myr) star formation and GALEX data (Thilker et al. 2005, Gil de Paz et al. 2007) to trace the recent (∼ 100 Myr) star formation. To trace the atomic gas, we use the HI 12″ resolution map published in Gratier et al. (2010), and for the molecular gas, their partial CO(2-1) 12″ resolution map (Gratier et al. 2010).

All useful characteristics of the images are summarized in Table 1. All maps have been deprojected, with the adopted inclination of 56° and position angle of 22.5°, before Fourier analysis.

The data analysed in the present work are more appropriate than earlier data (Elmegreen et al. 2003b, Odekon 2008, Sanchez et al. 2010) to study the power spectra and the structure of the interstellar medium, since they refer directly to the gas and dust in M33, and they have the dynamical range (from 40 pc to 20 kpc) and spatial resolution to reveal the thickness of the gas layer. The

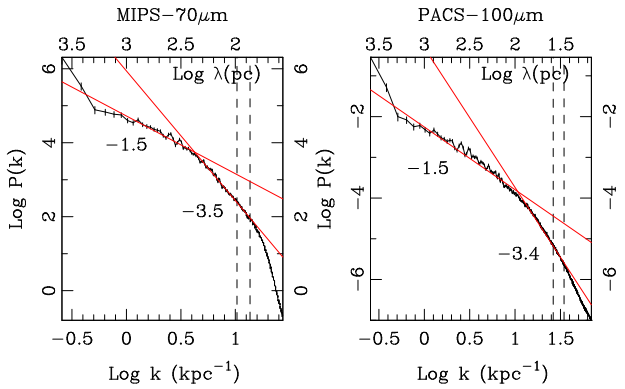

Fig. 3. Power spectrum of the Spitzer-MIPS 70μm map, and the PACS-100μm dust emission map of M33. The vertical dash line at right represents the spatial resolution of the observations, on the major axis. Since the de-projection to a face-on galaxy implies a factor 1/cos(56°) = 1.79 larger beam on the minor axis, we have also plotted a second dashed vertical line at left, indicating the geometric mean of the resolution on both minor and major axis. Statistical error bars are given in this first figure, and then omitted later for clarity. They are significant only at the largest scales (small k), where the statistical errors are the largest.

gas and dust emission trace directly the collisional material, with no intervening and perturbing emission (like galactic stars).

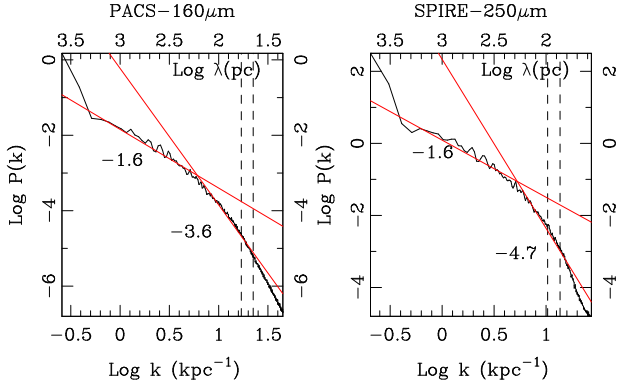

Fig. 4. Same as Figure 3, for the power spectrum of the PACS-160μm and SPIRE-250μm dust map.

3. Numerical model

In order to compare with what is expected from the dynamical instabilities of the interstellar medium, we have run idealised simulations, fitted for a late-type galaxy without bulge and rich in gas like M33.

3.1. Technique

The numerical code is based on the TREE/SPH version developed by Semelin & Combes (2005) and di Matteo et al. (2007), with star formation and feedback. The TREE gravitational part of the code deals with two collisionless components: the stars and the dark matter, which differ only by their initial conditions. It deals also with the gas component, whose hydrodynamics is

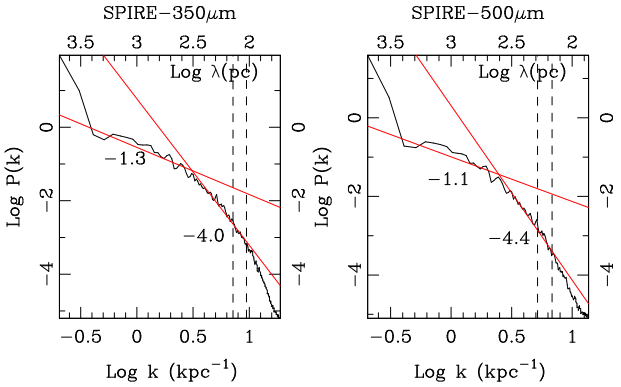

Fig. 5. Same as Figure 3, for the power spectrum of the SPIRE-350μm and 500μm cool dust map.

treated with the SPH (Smooth Particle Hydrodynamics) algorithm, using adaptive resolution. The softening parameter, or the spatial resolution of gravity, is taken to be 30 pc, and the average size of a gaseous particle (the SPH kernel, or spatial resolution of the hydrodynamics) is also around 30 pc, although it can drop down to 3 pc in overdense regions. The number of particles is 1.2 million, with 0.6 million gas particles, 0.4 million dark matter particles, and 0.2 million "stars" at the beginning of the simulations. The gas particles are assumed to follow an isothermal equation of state, with pressure forces corresponding to a sound velocity of 6 km s^{-1}, in the fiducial model. Shocks are treated with a conventional form of artificial viscosity, with parameters given in di Matteo et al. (2007). All physical quantities (density and forces) are computed averaging over a number of 50 neighbours. The equations of motion are integrated using a leapfrog algorithm with a fixed time step of 0.3 Myr.

Star Formation is taken into account in most models, with an assumed Schmidt law, of exponent n=1.5, i.e. for each gas particle of mass M_{gas}, and volumic density ρ_{gas} computed over its neighbours:

$$\frac{dM_{gas}}{M_{gas}dt} = C_* \rho_{gas}^{1/2}$$

where in most runs, the star formation constant C_* is calibrated such that the gas consumption time-scale is of the order of 2Gyr (then $C_* = C_0$). C_* is increased in some of the runs, to check its influence on the gas scale height. In most simulations, the density threshold for star formation is set very low, and is then increased in a few runs. Star formation is then taken into account for each gas particle, using the hybrid particles scheme (e.g. di Matteo et al. 2007), before sufficient stellar mass is accumulated and a star particle can be created. Continuous mass loss is also considered, with about 40% of the stellar mass loss by young massive stars after 5 Gyr (Jungwiert et al. 2001).

The energy reinjected by supernovae into the interstellar medium is assumed to be a kinematic feedback on neighboring gas particles: each neighbour of a SPH particle having formed δm of stars is given a radial kick in velocity away from the supernova formed. The energy available is computed from δm, assuming a Scalo IMF (about 0.5% of the stars formed have a mass larger than 8 M$_\odot$ and explode as supernovae), the energy of a supernova $E_{SN} = 10^{51}$ erg is distributed to the 50 neighbours according to their weight (the SPH kernel), with an efficiency ϵ, which has been varied from 10^{-4} to 1, with 10% being the fiducial value (see Table 2). For the fiducial feedback efficiency, a particle might get a kick of ~ 1 km s^{-1}at each time-step, for the extreme feedback, it can reach 5 km s^{-1}. The efficiency of the feedback is not well known, and depends on the coupling of the supernovae and the gas (whether the young stars have already left their birth clouds when they explode, etc..). Some energy and supernova explosions are also due to the old population of stars (e.g. Dopita 1985).

3.2. Initial conditions

The initial stellar component of the galaxy is selected to be of type Scd, similar to the M33 galaxy.

The stellar and gaseous disks are represented initially by Miyamoto-Nagai functions, with characteristic height parameters of 170 pc and 70 pc respectively. The stellar disk has a mass of 0.5×10^{10} M$_\odot$, with a characteristic radius of 2 kpc, while the gas disk has a mass of 1.5×10^9 M$_\odot$, with a radius 2.5 kpc. Both are embedded in a spherical halo of dark matter, represented by a Plummer sphere of mass 4×10^{10} M$_\odot$ within 18 kpc, with a characteristic radius of 9.5 kpc.

The initial stability of the gas and stellar disks is controlled by the Toomre parameter Q, ratio of the radial component of the velocity dispersion to the critical one $\sigma_{crit} = 3.36G\Sigma/\kappa$, Σ being the disk surface density of the component (gas or stars), and κ the epicyclic frequency. We select equal Toomre parameters for gaseous and stellar disks. The azimuthal velocity dispersions verify initially the epicyclic ratio $\sigma_\theta/\sigma_r = \kappa/2\Omega$, and the z-components are fixed by the isothermal equilibrium of the disks, in the vertical direction.

The gas is isothermal, but its equivalent velocity dispersion, governing the pressure, may be varied between 6 and 12 km s^{-1}. The recipes for star formation: efficiency, density threshold, and feedback, are also varied; they have a significant impact on the interstellar gas structure.

The initial conditions of the runs described here are given in Table 2. The rotation curve corresponding to one of the runs is plotted in comparison to the data points in Figure 1. All runs have similar rotation curves. Given the uncertainties, all the rotation curves are compatible with the data.

Table 2. Initial conditions of the simulations

Run	Q_* =Q_g	V_s (km/s)	C_*	threshold at. cm^{-3}	ϵ (feedback)
run1	2.	6.	C_0	2×10^{-6}	10^{-4}
run2	2.	6.	C_0	2×10^{-6}	10^{-3}
run3	2.	6.	C_0	2×10^{-6}	1.
run4	2.	6.	C_0	2×10^{-6}	10^{-1}
run5	1.5	6.	C_0x20	2×10^{-3}	10^{-1}
run6	1.	6.	C_0x20	4	10^{-1}
run7	1.	6.	0.	–	–
run8	1.	12.	0.	–	–
run9	1.	12.	C_0	2×10^{-6}	10^{-1}

C_0 is such that the gas depletion time is 2Gyr

4. Results

4.1. Power-spectrum of the data

The power spectra of the 2D projected maps were analysed through the 2D Fourier transform:

$$F^*(k_x, k_y) = \int_x \int_y F(x,y) e^{-i(k_x x + k_y y)} dxdy$$

where $F(x,y)$ is the intensity of each pixel, and k_x and k_y are the wave number, conjugate to x and y, varying as the inverse of scales. The full 2D power spectrum is given by

$$P(k_x, k_y) = (Re[F^*])^2 + (Im[F^*])^2$$

An example of 2D-power spectrum is given for the PACS-100μm image, in Figure 2. The one-dimensional power-spectrum $P(k)$ can be calculated through azimuthal averaging, in the (k_x,k_y) plane, using $k^2 = k_x^2 + k_y^2$. The power spectra $P(k)$ are plotted for the various maps in Figures 3, 4, 5, 6, 7 and 8. Two slopes have been fitted at small (ss) and large scales (LS), and the different values can be found in Table 3, together with the break scale separating the two regimes. In most of the cases, the power spectra show clearly two different regimes, with different slopes, and small and large-scales, for scales larger than the spatial resolution. A knee is apparent between the two regimes (ss and LS), and indicates the break scale. We have used a least-square-fit program to determine the slopes of the two power-laws, and left open the position of the separation between the two straight lines. Varying the value of the separation, we select for the break the value which minimises the sum of the χ^2 of the two line fits (ss and LS). In general the minimum is quite clear. There is one ambiguous case, however, which is the HI map, in Figure 8. The two slopes are close, and the determination less trustworthy. Examples of the deprojected images of the *Herschel* dust emission are displayed in Figures 9 and 10. In addition to the power spectra, the azimuthal large-scale structure develops spiral arms, that are quantified and studied in the Appendix A. The determination of the break scale is obviously more secure when it is found significantly larger than the resolution scale of the observations. We have tested the effect of spatial resolution by smoothing the PACS-100μm map in Appendix B. In the observed power spectra (e.g. Figures 3-7), the limit of the instrumental resolution is clearly seen, through the sudden change from a straight line to a dropping curve, at large k. We have indicated with two vertical dashed lines, the value of the resolution scale on the major axis, and also the geometric mean of the resolution on both minor and major axis, since the de-projection to a face-on galaxy implies a factor 1/cos(56°) = 1.79 larger beam on the minor axis. We conclude from Appendix B that break scales at least twice larger than the beam scale are robust with respect to resolution effect.

We have also tested the robustness of our determinations by computing the power spectra using only one side of the galaxy. The easiest way to compute that, with the same algorithm, was to remove in the map one half of the galaxy, say the southern part, and complete the map by extending the northern part by point symmetry through the center. For all maps, the different slopes and break scales for the two sides of the galaxy are also displayed in Table 3: the last columns display the extreme values found for the slopes and breaks. This procedure maximizes the error bars, especially in the LS-slopes, since the Norhern part of M33 is quite different from the Southern part. The slopes are determined with an error bar of the order of ±0.2 in general, and the break scales are even more robust, within 15%. We have also checked the effect of smoothing on the maps. As expected, the power-spectrum at large-scale is unchanged, and only the power at the extreme of the small-scales of the spatial resolution drops. The break scale also is enlarged by the resolution, when it is too close, and we can see for instance that the break at 70μm is larger than at 24 and 100μm (Table 3) only because of the coarser resolution. The fact that some maps have a pixel size smaller than the Nyquist size (half of the nominal resolution) does not influence the results. We have truncated the power spectra at the Nyquist sampling, in the figures.

Looking at Tables 1 and 3, it is ovious that the break scale is affected by the spatial resolution of the maps. Five maps have a ratio between break and resolution scales lower or equal to 3 (NUV, the 3 SPIRE, and CO), for the others, the ratio is 3.8 (FUV), 12.5 (Hα), 4.2 (MIPS-24μm), 3.9 (MIPS-70μm), 3.9 (PACS-100μm), 3.6 (PACS-160μm) and 3.3 (HI). For those, the determination of the break appears significant. As for the slope determination, the large-scale ones are not affected, and their variation is meaningful: the LS-slopes are flatter for the star-formation tracers than for the dust and gas, and they are growing steeper with wavelength.

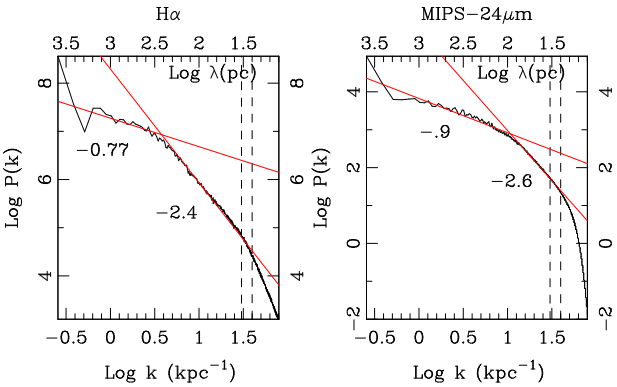

Fig. 6. Same as Figure 3, for the power spectrum of the Hα and MIPS-24μm maps.

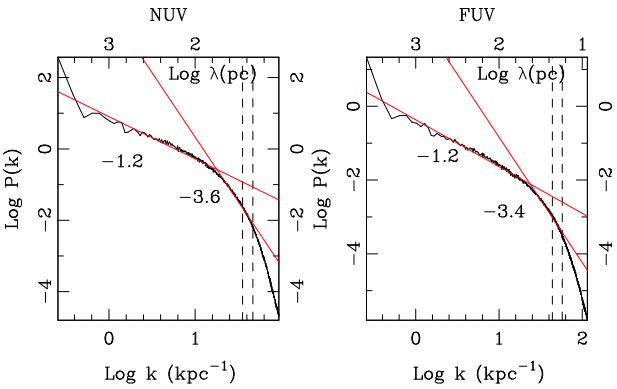

Fig. 7. Same as Figure 3, for the power spectrum of the GALEX NUV and FUV maps.

It is interesting to note that the Hα map, tracing gas ionized by the UV photons from massive stars and, indirectly, current star formation, has power spectrum slopes significantly flatter than the other power spectra of the ISM components. This might be expected, since star formation gives more power to the small scales. Its break scale, related to the plane thickness is higher. The GALEX FUV and NUV, tracing the recent, but past, star formation, have slopes more comparable to the other ISM slopes however, and have smaller break scales, implying thinner layers. The break scale in Hα is larger than in the UV because Hα traces the ionised gas, and only indirectly the young stars. The ionised layer may be thicker, affected by bubbles, filaments, fountain effects associated to star formation.

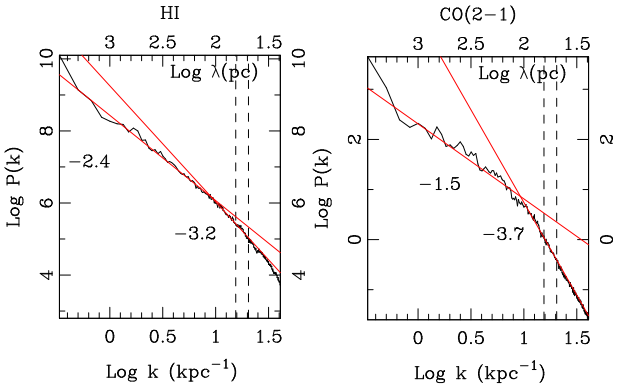

Fig. 8. Same as Figure 3, for the power spectrum of the HI and CO(2-1) maps.

Table 3. Power-law slopes and breaks for observations

Map	slope LS	slope ss	break (pc)	Extreme values LS	ss	(pc)
FUV	-1.2	-3.4	44	-0.9/-1.2	-3.4/-3.9	40-45
NUV	-1.2	-3.6	56	-1.0/-1.2	-3.0/-3.6	50-56
Hα	-.77	-2.4	300	-0.7/-1.0	-2.4/-2.7	250-300
24μm	-.9	-2.6	93	-0.9/-1.0	-2.6/-2.7	93-105
70μm	-1.5	-3.5	236	-1.4/-1.5	-3.4/-3.8	230-270
100μm	-1.5	-3.4	93	-1.4/-1.5	-3.2/-3.6	93-105
160μm	-1.5	-3.6	165	-1.5/-1.6	-3.6/-4.0	140-165
250μm	-1.6	-4.7	208	-1.4/-1.6	-4.3/-4.7	200-210
350μm	-1.3	-4.0	315	-1.3/-1.5	-4.0/-4.4	290-320
500μm	-1.1	-4.4	390	-1.1/-1.4	-4.2/-4.6	320-390
CO(2-1)	-1.5	-3.7	103	-1.3/-1.5	-3.6/-3.8	100-115
HI	-2.4	-3.2	110	-2.0/-2.4	-3.2/-3.6	100-120

LS= Large Scale (> 500 pc), ss= small scale (< 500 pc)

Table 4. Power-law slopes and breaks for simulations

Run	slope LS	slope ss	break (pc)	Comments	H_z (pc)
run1	-0.8	-3.6	75	low feedback	80
run2	-0.9	-3.4	75	"	80
run3	-2.3	-4.9	650	extreme feedback	217
run4	-1.3	-3.8	63	fiducial	120
run5	-2.1	-5.0	300	more SF (C*)	142
run6	-1.1	-4.0	430	higher threshold	103
run7	-0.8	-2.8	75	no SF	64
run8	-0.9	-2.9	201	no SF, Vs=12 km s^{-1}	110
run9	-1.1	-5.2	250	SF, Vs=12 km s^{-1}	108

LS= Large Scale, ss= small scale
The gas scale height $H_z = 2.35\ (< z^2 > - < z >^2)^{1/2}$

The dust emissions at various wavelengths have quite compatible power spectra. Their different break scales reflect the increasing beam size with wavelength. As for the gas, the molecular medium appears thinner than the atomic one, although spatial resolution might influence its break scale.

Independent of the spatial resolutions, the slope of the power-spectra at small scale are steeper at large wavelengths for the dust emission. Between 250 and 500μm, the SPIRE maps have slopes between -4.3 and -4.7, while the MIPS and PACS maps between 24 and 100μm have slopes comprised within -2.7 and -3.8. This is significant, and tends to show that the cool dust has less small-scale structure, since individual cloud cores are invisible.

4.2. Power-spectrum of the model

The various runs develop different gas structure and clumpiness, as can be seen in Figures 11 to 16, due to both initial conditions that are selected more or less stable, or with different sub-grid "temperature" of the gas, and to the star formation rate and feedback. Some galaxies, which are launched with initial conditions among the most stable, can end up with a more perturbed morphology and larger turbulence than others started more unstable, due to a larger supernovae feedback.

We computed the Fourier analysis in the same way on the gas maps obtained in the numerical simulations. The derived results are converging towards the same values at the middle of the runs, and we plot all of them for the final snapshots at T= 667 Myr for the sake of simplicity (cf Figures 17, 18 and 19). For comparison, we also plot the power-spectrum of some old stellar components, which have almost only one power-law (Figure 20). These correspond to run 2 and run 7 at T= 667 Myr. There is structure until about 300 pc, and no small-scale component, as expected for a collisionless component.

The first result which is obvious in Table 4 is that the predictions of the models bracket the values obtained in the observations, both in the slopes at large and small scales, and in the break scales. Those can be compared to the actual thickness of the gas layer, in the simulations. This is done in Table 4, showing that the break scale does not follow closely the thickness. Although both should be of the same order when only the self-gravity of the gas is taken into account, their close relation is blurred by other factors, and in particular the feedback efficiency. When the feedback is too extreme, the small scale structure of the gas is smoothed out, even towards larger scale than the vertical thickness. So the range of break scales is wider than that of possible plane heights.

The main parameters that control the turbulence and therefore the power-spectrum of the gas structure are the star formation rate, the amount of feedback, but also the assumed equivalent temperature of the gas, or sound speed, directly involved in the pressure forces. Increasing the turbulence by supernovae feedback suppresses efficiently the small-scale structure (power-law slopes of ~ -5.), and thickens substantially the gas layer, and the corresponding break scale. Without star formation and feedback, it is only possible to have gas morphologies comparable to the observed ones if a minimum sound speed of 12 km s^{-1}is injected. Figures 11 to 16 show the large variety of gas structures, according to the variations of those parameters. It appears that our fiducial model (run4) is the one which corresponds the best to the M33 galaxy, both for its morphology, and for the typical power-law slopes and break scale. It has a star formation rate of ~ 0.7 M$_\odot$/yr, and a feedback such that 10% of supernovae energy is coupled to the kinematics of the gas. Verley et al. (2009) found for M33 a star formation rate of 0.5 M$_\odot$/yr.

5. Discussion and conclusions

We have presented the Fourier analysis of dust and gas emission maps of M33 at several wavelengths, and compared them with the Hα and UV maps, tracers of recent star formation. We find that all the power spectra can be decomposed into two regimes, a large-scale (> 500 pc) power-law, of $-1.5 < \mathrm{slope}_{LS} < -1.0$, and a steeper small-scale one, with $-4.0 < \mathrm{slope}_{ss} < -3.0$.

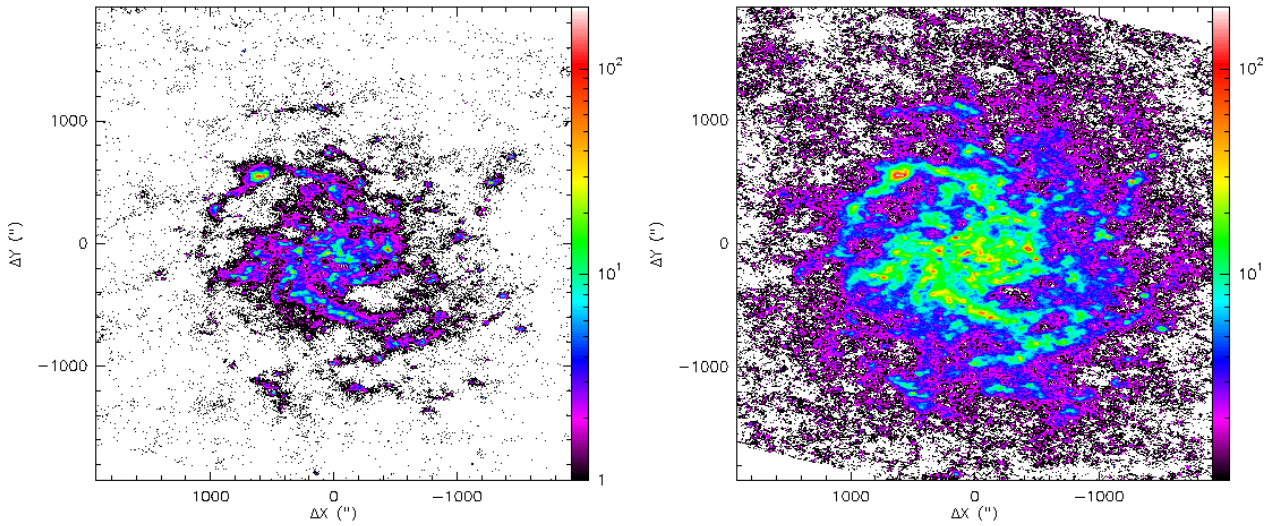

Fig. 9. Deprojected maps of the dust at 100 (left) and 160μm (right). The major axis has been rotated to be vertical. The color scale is in arbitrary units.

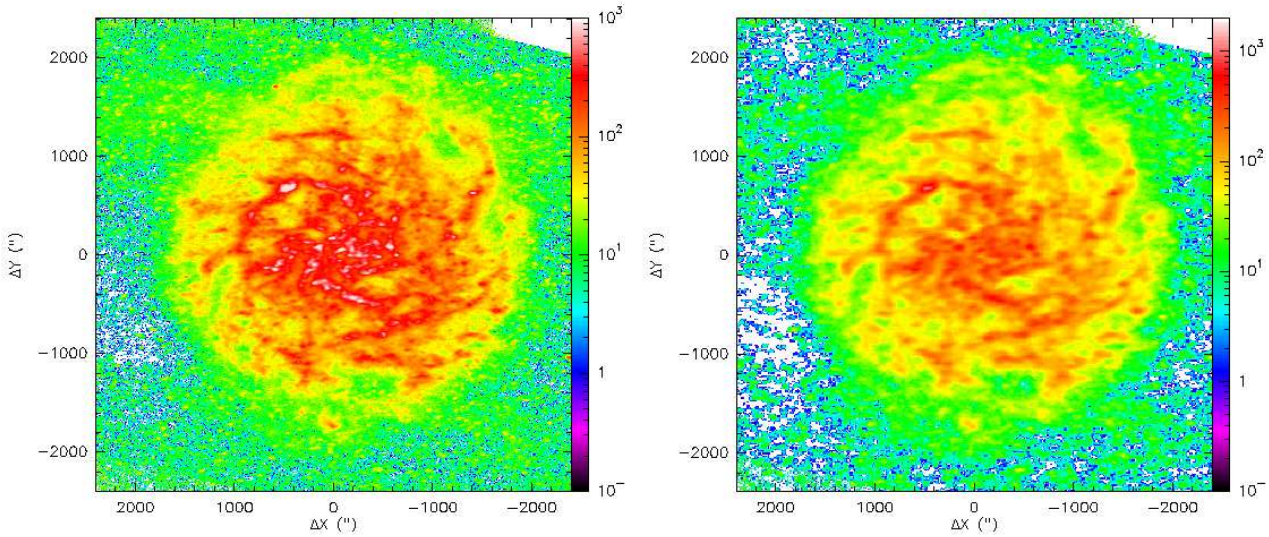

Fig. 10. Deprojected maps of the dust at 250 (left) and 500μm (right). The major axis has been rotated to be vertical. The color scale is in arbitrary units.

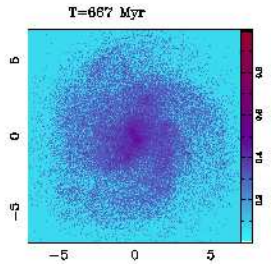

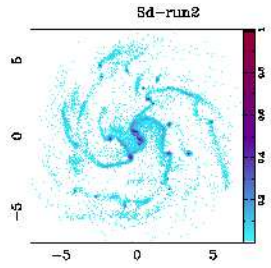

Fig. 11. Face-on projection of the run2 model, at T=667 Myr. **Left** are the stars, and **Right**, the gas. The linear scales on both axes are in kpc, and the color scale is in arbitrary units.

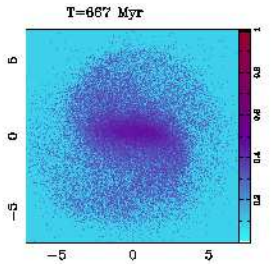

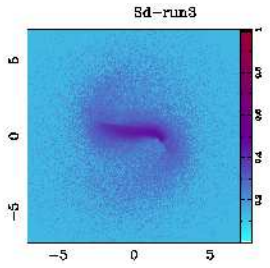

Fig. 12. Face-on projection of the run3 model, at T=667 Myr. **Left** are the stars, and **Right**, the gas. The linear scales on both axes are in kpc, and the color scale is in arbitrary units.

The latter slopes correspond quite well to what is found for the Milky Way (Dickey et al. 2001) or the Small Magellanic Cloud (Stanimirovic et al. 2000). The Hα star formation tracer has shallower power-spectra, indicating more power at small scales. The break scale is of the order of 100-150 pc for the dust and the gas, increasing at large wavelength, probably influenced by the

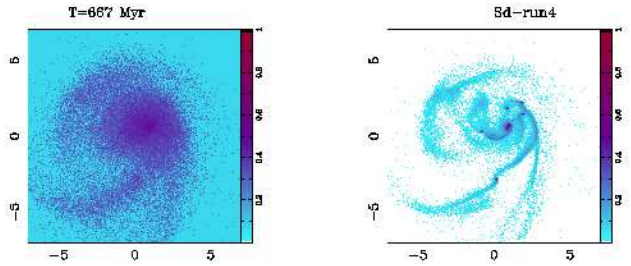

Fig. 13. Face-on projection of the run4 model, at T=667 Myr. **Left** are the stars, and **Right**, the gas.

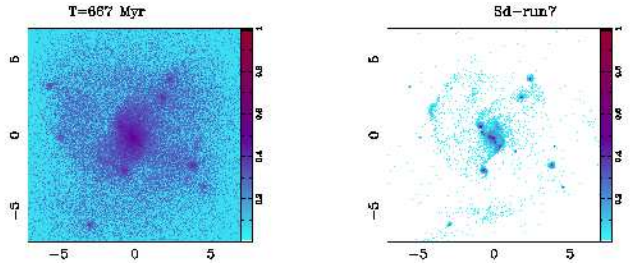

Fig. 14. Face-on projection of the run7 model, at T=667 Myr. **Left** are the stars, and **Right**, the gas.

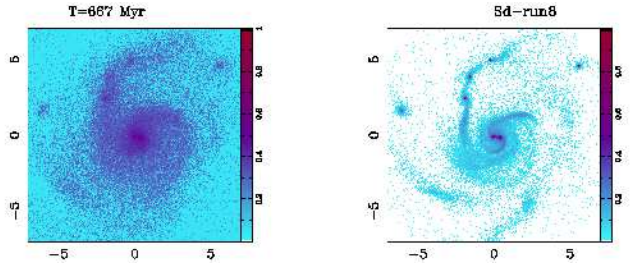

Fig. 15. Face-on projection of the run8 model, at T=667 Myr. **Left** are the stars, and **Right**, the gas.

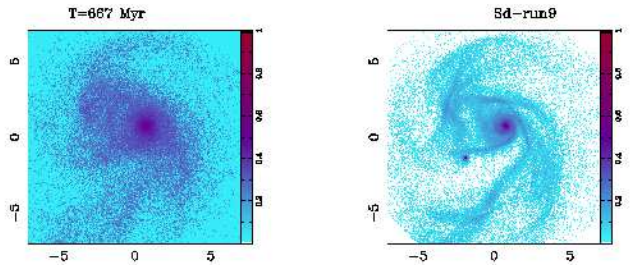

Fig. 16. Face-on projection of the run9 model, at T=667 Myr. **Left** are the stars, and **Right**, the gas.

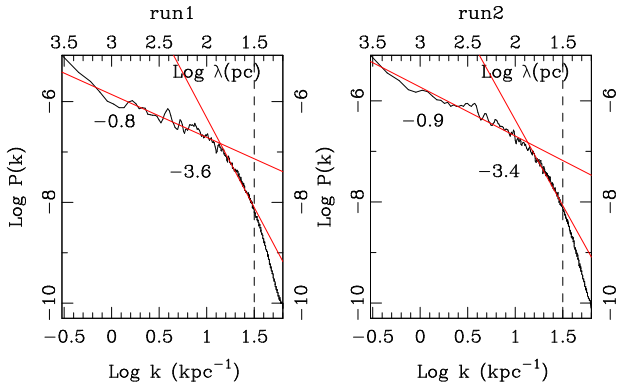

Fig. 17. Power spectrum of the gas in models run1 and run2. The vertical dash line represents the softening length of the gravity.

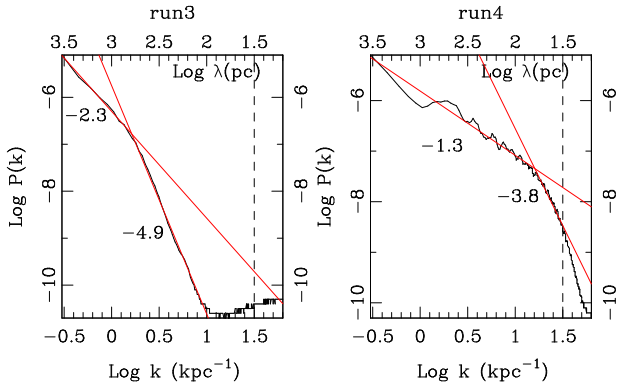

Fig. 18. Power spectrum of the gas in models run3 and run4.

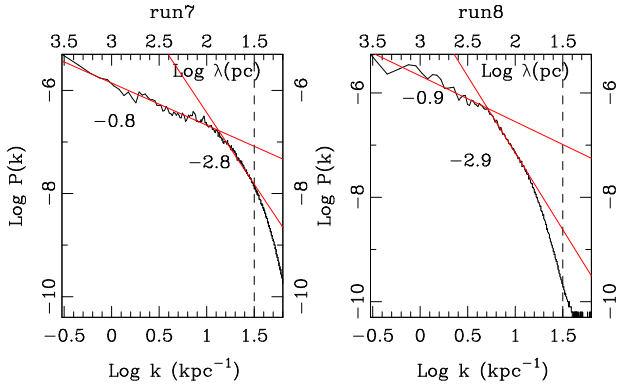

Fig. 19. Power spectrum of the gas in models run7 and run8.

progressive lack of spatial resolution. The Hα break scale is significantly higher (300 pc), implying a thicker layer for ionized gas, while the UV layers appears thinner (65 pc). This might be understood considering that UV originates from stars that are concentrated in the disk whereas the ionised gas could be present quite far from the plane of the disk: giant HII regions have typically round shapes, and are not as confined to the disk. Tabatabaei et al. (2007) have already shown with wavelets that the Hα map is dominated by giant HII regions, which are bubble-like with sizes from 100 to 500 pc. By comparison the diffuse component is weaker, which flattens the Fourier ss-slope, and enlarges the break scale. Although the warm dust in the MIPS-24μm map is also related to the young star formation, there are no such large bubbles: only the point sources are prominent inside the bubble, as can be seen in Figure 3 of Verley et al. (2010). This explains the different break scales between Hα and MIPS-24μm maps.

It is also possible that the large thickness suggested by the Hα analysis is related to the diffuse ionized gas (DIG) observed in several edge-on galaxies to follow a rather thick layer of about 1 kpc height (see a review by Dettmar 1992). This extra-planar ionized gas is thought to be due to star formation, it is present in about 40% of 74 edge-on galaxies (Rossa & Dettmar 2003). It can be widely diffuse, or take the shape of filaments, plumes and bubbles (Rand, 1997). These extra-planar extensions could be due to UV ionizing photons escaping the star forming regions, supernovae feedback, fountain effects, chimneys, and be part of

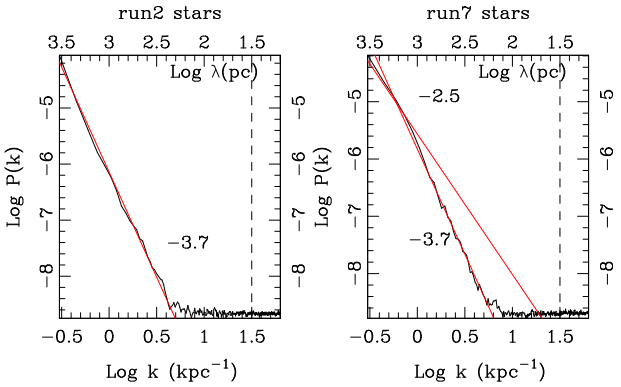

Fig. 20. Power spectrum of the stellar component in run2 and run7. The vertical dash line represents the softening length of the gravity.

an active disk-halo interaction, with exchange of matter (Howk & Savage 2000).

The comparison with simulated models tells us that the observation of a break in the power-spectrum of observed gas distribution is not always related to the 2D/3D transition, and indicates the thickness of the gaseous disk only when the latter is not heated by a strong star formation rate and a strong supernovae feedback. For a quiescent galaxy, the break should still be an indication of the gas layer thickness.

Block et al. (2010) found in the LMC that the small scale slopes of the power spectra were steeper at longer wavelengths, i.e. the cool dust was smoother than the hot emission. We find a similar result. The slope of the SPIRE maps are around -4.5, while the warmer dust at 24-100μm has an average slope of -3.2. This observation can be interpreted in terms of star formation occuring in the clumpy medium. Once the stars are formed, they heat the dust around, and this explains why the emission at shortest wavelength (warmer dust) is more clumpy. Also the break scale, and thus the thickness of the plane, is larger for the cold gas. This could be due in addition to the fact that the cold component is much more extended in radius (Kramer et al. 2010), and it is well known that the gas layer is flaring in the outer parts of galaxies. As for the gas emission, the molecular gas appears more clumpy, but only slightly more so than the atomic gas. And the break occurs at about the same scale. Since it is likely that in the relatively quiescent M33 galaxy, the break indicates the thickness of the gas layer, this situation is not alike the Milky Way, where the CO component is significantly thinner than the HI (Bronfman et al. 1988). A thick CO layer, 3 times as wide as the dense molecular gas layer, and comparable to the HI layer, has been observed (Dame & Thaddeus 1994), but it involves a small mass. M33 being a galaxy of intermediate mass, could have indeed a thicker gas layer than the Milky Way (Dalcanton et al. 2004).

We also showed that numerical models predict gas morphologies and small scale power-laws which bracket the observational data. It is possible to obtain a colder or a more turbulent interstellar medium, by varying the star formation feedback and the sound speed of the gas. The Fourier analysis of the models reveals that the break scale is a good indicator of the actual thickness of the gas layer, although it varies within a wider range when extreme feedback is used, and smoothes out the small scale gas structures. The power-law slopes obtained in the models at large and small scale reflect quite accurately the gas morphology and turbulence. Fourier analyses are therefore a good tool to determine the thickness of the gas plane, at any orientation on the plane of the sky, and the actual physical state of the gas, in its star formation phase. Note however that the current models are not devoid of shortcomings: they only partly allow to distinguish between the 12 different tracers of the gas phase observed here, as radiative transport, dust properties, etc. are not taken into account.

Comparison of power spectrum analysis between galaxies should allow a determination of their relative star formation rate and feedback. This will need however high spatial resolution maps, such as the ones that will be provided with ALMA.

The gas plane in M33 appears relatively thick and turbulent, with respect to our closest fiducial model, which could be a consequence of its recent heating in particular through the M31 interaction (McConnachie et al. 2009).

Acknowledgements. We warmly thank the anonymous referee for his/her constructive comments and suggestions. We have made use of the NASA/IPAC Extragalactic Database (NED).

References

Begum, A., Chengalur, J. N., Bhardwaj, S.: 2006, MNRAS 372, L33
Bianchi S., Xilouris E. M.: 2011, A&A 531, L11
Block D. L., Puerari, I., Elmegreen, B. G., Bournaud, F.: 2010 ApJ 718, L1
Boquien E., Calzetti, D., Kramer, C. et al. : 2010, A&A 518, L70
Boquien E., Calzetti, D., Combes F. et al. : 2011 AJ 142, 111
Bournaud, F., Combes, F., Jog, C. J., Puerari, I.: 2005, A&A 438, 507
Bournaud F., Elmegreen, B. G., Teyssier, R., Block, D. L., Puerari, I.: 2010, MNRAS 409, 1088
Braine J., Gratier P., Kramer C. et al. : 2010, A&A 518, L69
Bronfman L, Cohen R.S., Alvarez H et al. , 1988, ApJ 324, 248
Corbelli E., Salucci P.: 2007, MNRAS 311, 441
Crovisier J., Dickey J.: 1983 A&A 122, 282
Dalcanton J.J., Stilp A.M.: 2010, ApJ 721, 547
Dalcanton J.J., Yoachim P., Bernstein R.: 2004, ApJ 608, 189
Dame T.M., Thaddeus P., 1994, ApJ 436, L173
Dettmar R.J.: 1992, Fund. Cosmic Physics, 15, 143
Di Matteo P.,, Combes F., Melchior A.-L., Semelin B.: 2007, A&A 468, 61
Dickey, J. M., McClure-Griffiths, N. M., Stanimirovic, S., Gaensler, B. M., Green, A. J.: 2001 ApJ 561, 264
Dopita M.A.: 1985 ApJ 295, L5
Dutta P., Begum, A., Bharadwaj, S., Chengalur, J. N.: 2008 MNRAS 384, L34
Dutta P., Begum, A., Bharadwaj, S., Chengalur, J. N.: 2009a MNRAS 397, L60
Dutta P., Begum, A., Bharadwaj, S., Chengalur, J. N.: 2009b MNRAS 398, 887
Elmegreen B.G., Kim, S., Staveley-Smith, L.: 2001 ApJ 548, 749
Elmegreen B.G., Leitner, S. N., Elmegreen, D. M., Cuillandre, J-C.: 2003b ApJ 593, 333
Elmegreen B.G., Elmegreen D.M., Leitner, S. N.: 2003a, ApJ 590, 271
Elmegreen B.G., Scalo J.: 2004, ARAA 42, 211
Elmegreen B.G., Elmegreen, D. M., Chandar, R., Whitmore, B., Regan, M.: 2006 ApJ 644, 879
Falgarone E., Phillips, T.G., Walker C.K.: 1991, ApJ 378, 186
Freedman, W. L.,Wilson, C. D., Madore, B. F. 1991, ApJ, 372, 455
Gil de Paz, A., Boissier, S., Madore, B. F., et al. : 2007, ApJS, 173, 185
Goldman I.: 2000 ApJ 541, 701
Gratier, P., Braine, J., Rodriguez-Fernandez, N. J., et al. 2010, A&A, 522, A3
Green D.A.: 1993, MNRAS 262, 327
Hoopes C.G., Walterbos R.A.M., Bothun G.D.: 2001, ApJ 559, 878
Howk J.C., Savage B.D.: 2000, AJ 119, 644
Jungwiert B., Combes F., Palous J.: 2001, A&A 36, 85
Khalil, A., Joncas, G., Nekka, F., Kestener, P., Arneodo, A.: 2006, ApJS 165, 512
Kramer, C. Buchbender, C., Xilouris, E.M. et al. : 2010, A&A 518, L67
Lazarian, A., Pogosyan, D.: 2004, ApJ 616, 943
Lazarian, A., Pogosyan, D., Vzquez-Semadeni, E., Pichardo, B.: 2001 ApJ 555, 130
McConnachie A.W., Irwin, M. J., Ibata, R. A. et al. 2009, Nature 461, 66
Odekon M. C.: 2008 ApJ 681, 1248
Padoan P., Kim, S., Goodman, A., Staveley-Smith, L.: 2001 ApJ 555, L33
Pfenniger D., Combes F.: 1994, A&A 285, 94
Rand, R.J.: 1997, ApJ 474, 129
Rossa J., Dettmar R.J.: 2003, A&A 406, 493

Roychowdhury, S., Chengalur, J. N., Begum, A., Karachentsev, I. D.: 2010, MNRAS 404, L60
Sanchez N., Anez, N., Alfaro, E. J., Crone Odekon, M.: 2010 ApJ 720, 541
Semelin B., Combes F.: 2005, A&A 441, 55
Stanimirovic S., Lazarian A.: 2001, ApJ 551, L53
Stanimirovic S., Staveley-Smith, L., van der Hulst, J. M. et al. 2000: MNRAS 315, 791
Stutzki, J., Bensch, F., Heithausen, A., Ossenkopf, V., Zielinsky, M.: 1998, A&A 336, 697
Tabatabaei F.S., Beck R., Krause M. et al. : 2007, A&A 466, 509
Thilker, D. A., Hoopes, C. G., Bianchi, L. et al. : 2005, ApJ 619, L67
Verley, S., Hunt, L. K., Corbelli, E., Giovanardi, C.: 2007, A&A, 476, 1161
Verley S., Corbelli, E., Giovanardi, C., Hunt, L. K.: 2009, A&A 493, 453
Verley S., Relano, M., Kramer, C. et al. : 2010, A&A 518, L68

Appendix A: Fourier analysis of the density

Until now, we have essentially analysed the small scale structure of the interstellar medium in various tracers, but ignored the azimuthal dependence. The different tracers also reveal a contrasted spiral structure, that is interesting to present, at least in two representative deprojected maps, the *Herschel* 100μm image (dust and gas images show similar features), and the Hα image (star formation, similar to UV images).

We have computed the Fourier transform of the corresponding surface densities, decomposed as:

$$\mu(r,\phi) = \mu_0(r) + \sum_m a_m(r)\cos(m\phi - \phi_m(r))$$

where the normalised strength of the Fourier component m is $A_m(r) = a_m(r)/\mu_0(r)$. Thus, A_2 represents the normalized amplitude for a $m = 2$ distortion like a bar or spiral arm, at a given radius, and A_1 represents the same for the disk lopsidedness. The quantity ϕ_m denotes the position angle or the phase of the Fourier component m. Such a density analysis has been made for example by Bournaud et al. (2005), to study asymmetries and lopsidedness in galaxies, and correlate it with $m = 2$ features.

Figure A.1 shows a plot of the amplitude $A_m(r)$ and the phase $\phi_m(r)$ versus radius r for M33, at 100μm and Figure A.2, the same for Hα. Both show a prominent spiral feature at radii ~ 3-4 kpc, with a phase decreasing slightly with radius, in the direct sense. The $m = 2$ distortions show accompanying $m = 4$ harmonics. The lopsidedness also increases with radius, while the the corresponding phase is fairly constant.

These plots show that the spiral structure in M33 is mildly contrasted, in both gas and SFR tracers. Indeed, the normalised $m = 2$ amplitude is between 0.4 and 0.8. There is also a significant asymmetry and lopsidedness, as testified by the strong $m = 1$ amplitude comparable with the $m = 2$. This explains why the slopes at large-scale were more different between the two halves of the galaxy than the small-scale ones. This large asymmetry could be due to the current interaction between M33 and M31 (McConnachie et al. 2009).

Appendix B: The effect of resolution

We have explored the effect of spatial resolution in the determination of the various slopes and break scales, in smoothing the PACS-100μm map at various resolutions, from the original 7″ to 11, 18, 26 and 36″, corresponding to 44, 72, 104 and 144 pc on the major axis. The resulting fits are shown in Figure B.1 and B.2, to be compared with Figure 3. The break scales are respectively 97, 111, 135, 195 pc, instead of 93 pc for the original 7″ resolution. The determination is possible only for the two first cases.

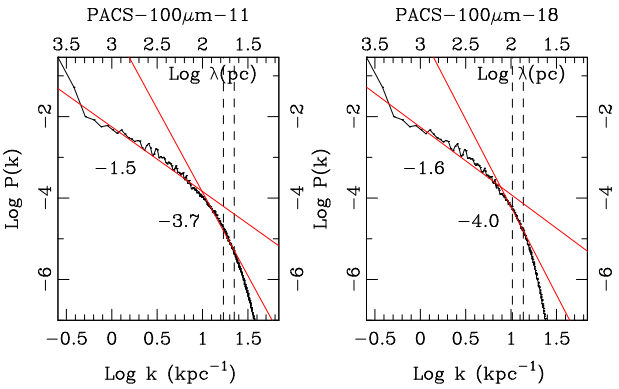

Fig. B.1. Power spectrum of the PACS 100μm map, at degraded resolutions of 11 and 18″. The vertical dash line at right represents the smoothed spatial resolution, on the major axis. Since the de-projection to a face-on galaxy implies a factor 1/cos(56°) = 1.79 larger beam on the minor axis, we have also plotted a second dashed vertical line at left, indicating the geometric mean of the resolution on both minor and major axis.

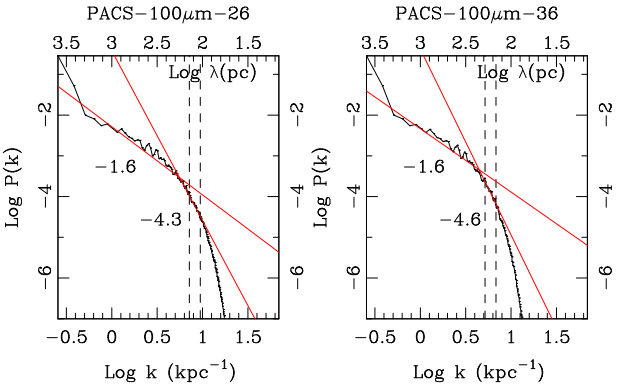

Fig. B.2. Same as Figure B.1 for the degraded resolutions of 26 and 36″.

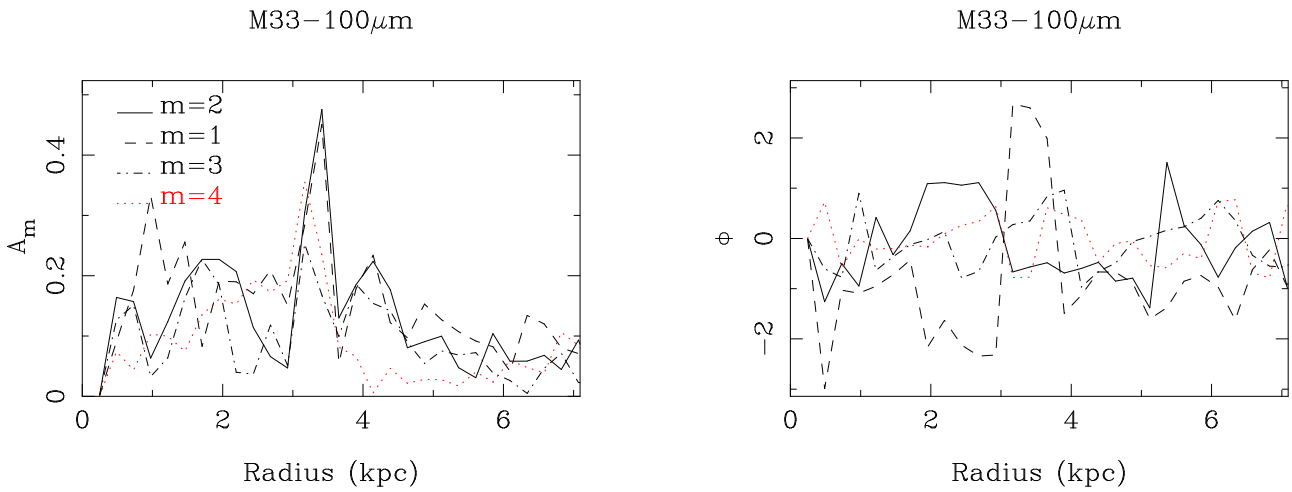

Fig. A.1. Left: Radial variations of A_m, for $m = 1 - 4$, the normalised Fourier amplitudes of the deprojected 100μm image of M33. **Right**: Corresponding radial variations of the phases Φ_m in radians.

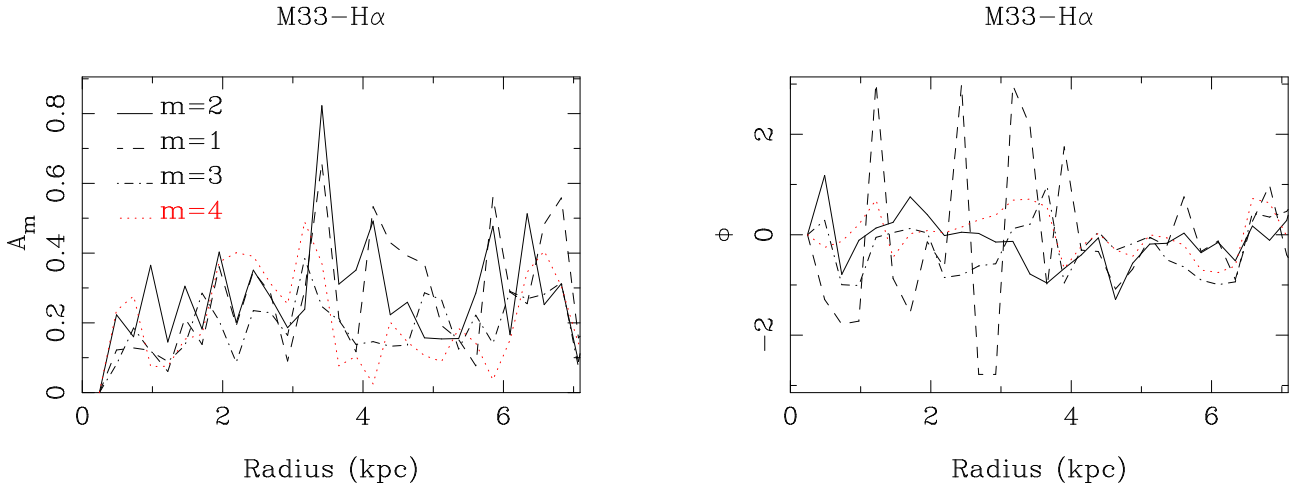

Fig. A.2. Left: Radial variations of A_m, for $m = 1 - 4$, the normalised Fourier amplitudes of the deprojected Hα image of M33. **Right**: Corresponding radial variations of the phases Φ_m in radians.